optica

Varifocal zoom imaging with large area focal length adjustable metalenses: supplementary material

SHANE COLBURN,[1] ALAN ZHAN,[2] ARKA MAJUMDAR,[1,2,*]

[1]Department of Electrical Engineering, University of Washington, Seattle, Washington 98195, USA

[2]Department of Physics, University of Washington, Seattle, Washington 98195, USA

*Corresponding author: arka@uw.edu

Published 10 July 2018

This document provides supplementary information to "Varifocal zoom imaging with large area focal length adjustable metalenses," https://doi.org/10.1364/OPTICA.5.000825.

S1. Materials and Methods

A. Simulation and Design

The silicon nitride nanoposts were simulated using the Stanford S4 rigorous coupled-wave analysis (RCWA) package **[1]**. The validity of the unit cell approximation was evaluated by calculating the transmission amplitude and phase as a function of both diameter and lattice constant. For our 1550 nm simulation, we set the refractive indices of silicon and silicon nitride to 3.476 and 1.996 respectively. For our 633 nm simulation, we set the refractive indices of silicon dioxide and silicon nitride to 1.457 and 2.039 respectively. Subsequent metasurface designs were evaluated as complex amplitude masks based on the RCWA data and simulated by evaluating the Rayleigh-Sommerfeld diffraction integral by means of an angular spectrum propagator.

B. Fabrication

We used a dictionary of 6 fixed nanopost designs to make a hierarchy of cell references when generating our metasurfaces' layout file to substantially cut the required memory. Our process began with either a 100 mm silicon or quartz wafer, depending on whether the infrared or visible lens design was being fabricated. Using a SPTS Delta PECVD system, we deposited 2 μm of silicon nitride at 350 °C and a chamber pressure of 5 mTorr at a deposition rate of 25 nm/min, based on a gas mixture of N_2, H_2, N_2O, SiH_4, NH_3, and Ar. Our reticle was fabricated by Toppan Photomasks, Inc. and we transferred our pattern onto a film of AZ Mir 701 11 cps spun on top of the silicon nitride layer using a 5x reduction stepper lithography system (Canon FPA-3000 i4). After development in AZ 300, we evaporated and then lifted off a 150 nm layer of aluminum to form a hard mask. We then etched the exposed nitride layer using a PlasmaLab 100 ICP-180 inductively-coupled plasma etcher system. Our recipe exhibited a silicon nitride etch rate of ~330 nm/min, relying on a chemistry of 3.0 sccm of SF_6 and 13.3 sccm of CHF_3, a chamber pressure of 5.0 mTorr, temperature of -7 °C, and ICP and RF powers of 1250 W and 50 W respectively. We removed the remaining aluminum by etching in AD-10 photoresist developer. To capture the scanning electron micrographs, we sputtered an 8 nm Au/Pd film as a charge dissipation layer, which was subsequently removed using type TFA gold etchant.

C. Focal Length Measurement

To measure the focal length of our 1550 nm metalens, we imaged the focal plane of the tunable metalens with a custom microscope positioned on a motion-controlled stage. We illuminated the whole aperture of the lens by passing a fiber-coupled and collimated 1550 nm SLD through a beam expander and adjusted the displacement of each plate by means of separate translation stages, projecting the microscope image of the focal plane onto an InGaAs camera [Fig. S2(a)]. To characterize the focal length of the 633 nm lens, we illuminated the device with a HeNe laser passed through a beam expander, actuated the plates with micrometer translations stages, and measured the focal length with a meterstick [Fig. S2(b)].

D. Imaging with the metalens

To image with our device, we illuminated our test patterns with a 625 nm LED, placed the tunable lens in the optical path at the fixed object distance, and tuned the focal length with translation stages to project the image directly onto a CCD camera [Fig. S3]. To zoom, we tuned the focal length of

our metalens and shifted the CCD camera to the image plane. We imaged both by illuminating patterns in transmission and by scattering light off printed object patterns.

E. Efficiency Measurements

To measure the focusing efficiency of the lenses, we took the ratio of the optical power measured with a power meter (Newport Model 843-R) at the focal plane to that measured near the surface of the lens after transmission. In the case of the 633 nm efficiency measurement with the quartz substrate design, due to the super-wavelength lattice constant and higher diffraction orders which we could not capture with our power meter, we defined our focusing efficiency as the ratio of the focal plane power to that which passes through two glass plates with quartz substrates mounted on each with the same orientation and separation distance as our Alvarez lens setup. In using these glass plates and quartz substrates without any nitride patterning, this provides an underestimate of the focusing efficiency as the patterned nitride layer would induce further reflections and scattering, reducing the total optical power transmitted through the lens surface. The zeroth order beam efficiency of the metalens is defined as the ratio of the focal plane power to that measured passing through the metalens surface itself with the higher diffraction orders not being captured by the power meter.

S2. Characterization of lenses and vortex beam generators based on the silicon nitride nanopost platform

In addition to the designed metasurface Alvarez lenses of the main text, to further demonstrate the versatility of our nanopost design and fabrication process, our reticle also included several static singlet and vortex beam-generating metalenses for 1550 nm operation. Fig. S1 summarizes the data collected in characterizing these devices, demonstrating successful focusing at the design focal length [Fig. S1(a)-(b)] and orbital angular momentum generation for different values of topological charge [Fig. S1(c)]. Our designed 2 mm static focal length lens exhibited close to diffraction-limited performance with a spot size of 3.94 μm, near the diffraction-limited value of 3.2 μm. The success of these devices verified the behavior and fabrication of the designed dielectric scatterers using our stepper lithography-based platform.

S3. Setup for measuring the focal length of the tunable metalens system

To measure the focal length of our metalens system, we had to illuminate our device with light passed through a beam expander (Thorlabs BE10M-A) to illuminate the full aperture of the metalens. In the case of the infrared design, we used a microscope on a motioned-controlled stage to image the focal plane of the metalens system (Fig. S2A). This microscope comprised an objective lens (Nikon Plan Fluor 20x/0.50, DIC M, ∞/0.17, WD 2.1), tube lens (Thorlabs ITL200), and camera (Xenics Bobcat-1.7-320). By laterally actuating the metasurface plates by means of translation stages, the focal length of the system would shift and we could translate the microscope until it was in focus and use the displacement to calculate the focal length. For the visible design, with the larger focal range supported by our device, it was beyond the range of our motion controlled-stage and microscope, so we used a reflective screen and meterstick to measure the focal length (Fig. S2B). For the infrared design, we used a 1550 nm SLD (Thorlabs S5FC1005P) and for the visible design we used a HeNe laser as our illumination source.

S4. Setup for imaging in transmission and scattering modes

To image patterns with our metalens system, we illuminated objects in transmission (Fig. S3A) and by scattering light off printed object patterns with off-axis illumination (Fig. S3B) using a 625 nm LED (Thorlabs M625F2). Without additional optical elements in the path, we adjust the focal length of our metalens with translation stages to project an image of the object pattern directly onto a camera (AmScope MU300).

S5. Layout file generation algorithm

In our algorithm, we use a dictionary data structure containing 6 unique nanopost radii as keys, each of which maps to a unique 32-sided regular polygon cell which approximates a circle. The 6 possible key-value pairings correspond to 6 possible discrete phase shifts in the 0 to 2π range to reduce the required memory, as opposed to utilizing a continuous spectrum of diameters. In generating the file, we iterate through a list of diameters and positions describing our layout and instantiate the appropriate cell reference for each nanopost by accessing our dictionary with the nanopost's radius key, as opposed to making a separate cell for each nanopost. In the case of our metasurface Alvarez lens metasurface plates, we cut the memory from 372 GB to 4.4 GB as a GDSII, and to only 140 MB as an OASIS file (more than a 2600x reduction).

S6. Effect of lateral misalignment on Alvarez metalens performance

The two cubic phase metasurfaces comprising the Alvarez metalens system should be laterally actuated by the same distance in opposite directions. In the case, however, where there is a lateral misalignment error, the system will still focus but will undergo both a longitudinal shift of the focal plane and a lateral shift of the focal spot as well. This behavior is evident in the blurring and lateral shift of the Air Force resolution test images in Fig. 4(b) of the main text. To understand this behavior, we can derive the system's phase function when one of the cubic phase plates is laterally misaligned by a distance ε. Following from equations (1) and (2) of the main text, we can write the system's phase as below

$$\begin{aligned}\boldsymbol{\varphi}(\mathbf{x},\mathbf{y}) &= \boldsymbol{\varphi}_{\mathbf{reg}}(\mathbf{x}+\mathbf{d},\mathbf{y}) + \boldsymbol{\varphi}_{\mathbf{inv}}(\mathbf{x}-\mathbf{d}-\boldsymbol{\varepsilon},\mathbf{y}) \\ &= \mathbf{A}(2\mathbf{d}+\boldsymbol{\varepsilon})(\mathbf{x}^2+\mathbf{y}^2) - \mathbf{A}\boldsymbol{\varepsilon}(2\mathbf{d}+\boldsymbol{\varepsilon})\mathbf{x} \\ &\quad + \mathbf{A}\left(\frac{2}{3}\boldsymbol{d}^3 + \boldsymbol{d}^2\boldsymbol{\varepsilon} + \boldsymbol{d}\boldsymbol{\varepsilon}^2 + \frac{\boldsymbol{\varepsilon}^3}{3}\right)\end{aligned}$$

Eliminating constant phase terms, we can write the system's phase function as below

$$\boldsymbol{\varphi(x,y) = A(2d+\varepsilon)(x^2+y^2) - A\varepsilon(2d+\varepsilon)x}$$

Here, we can consider the phase as a superposition of two different elements, the first term being for a lens with a focal length given by

$$\boldsymbol{f(d) = \frac{\pi}{\lambda A(2d+\varepsilon)}}$$

We see that this focal length is like that of equation (3) in the main text, except that the scaling by the ε misalignment distance longitudinally shifts the focal plane. The second term of the system's phase is a linear phase ramp in *x* for a beam deflector for which the deflection angle can be calculated via the generalized law of refraction **[2]**:

$$\boldsymbol{n_t \sin\theta_t - n_i \sin\theta_i = \frac{\lambda_0}{2\pi}\frac{d\Phi}{dx}}$$

Assuming we are in vacuum ($\boldsymbol{n_t = n_i = 1}$), normal incidence ($\boldsymbol{\theta_i = 0}$) and plugging in the second term of our phase function for $\boldsymbol{\Phi}$ and solving for θ_t gives

$$\boldsymbol{\theta_t = -\sin^{-1}\left[\frac{\lambda_0 A\varepsilon(2d+\varepsilon)}{2\pi}\right]}$$

In conjunction, the effect of these two phase-functions is to both laterally shift and blur the images in Fig. 4(b) of the main text.

S7. DUV Lithography-compatible subwavelength silicon nitride nanopost design for visible operation

The demonstrated visible lens design of the main text was based on a nanopost design with a lattice constant which was greater than the operating wavelength of 633 nm. This high lattice constant was used to enable fabrication with the stepper lithography system available in our university's cleanroom. State-of-the-art deep UV lithography systems, however, can achieve feature sizes down to 50 nm and as such much lower lattice constants are achievable in practice. To demonstrate the versatility of the tested silicon nitride platform and to show that fabricating subwavelength nanoposts for visible light is well within the means of existing fabrication tools, we have provided an alternative silicon nitride nanopost on quartz design. This design is based on a periodicity of 443 nm, and post thickness and operating wavelength of 633 nm. The RCWA-simulated transmission coefficient is provided in Fig. S4. The transmission coefficient exhibits 2π phase coverage with near unity amplitude. The diameters of the nanoposts (ranging between 125 nm to 400 nm) can be selected off resonance to ensure higher efficiency operation.

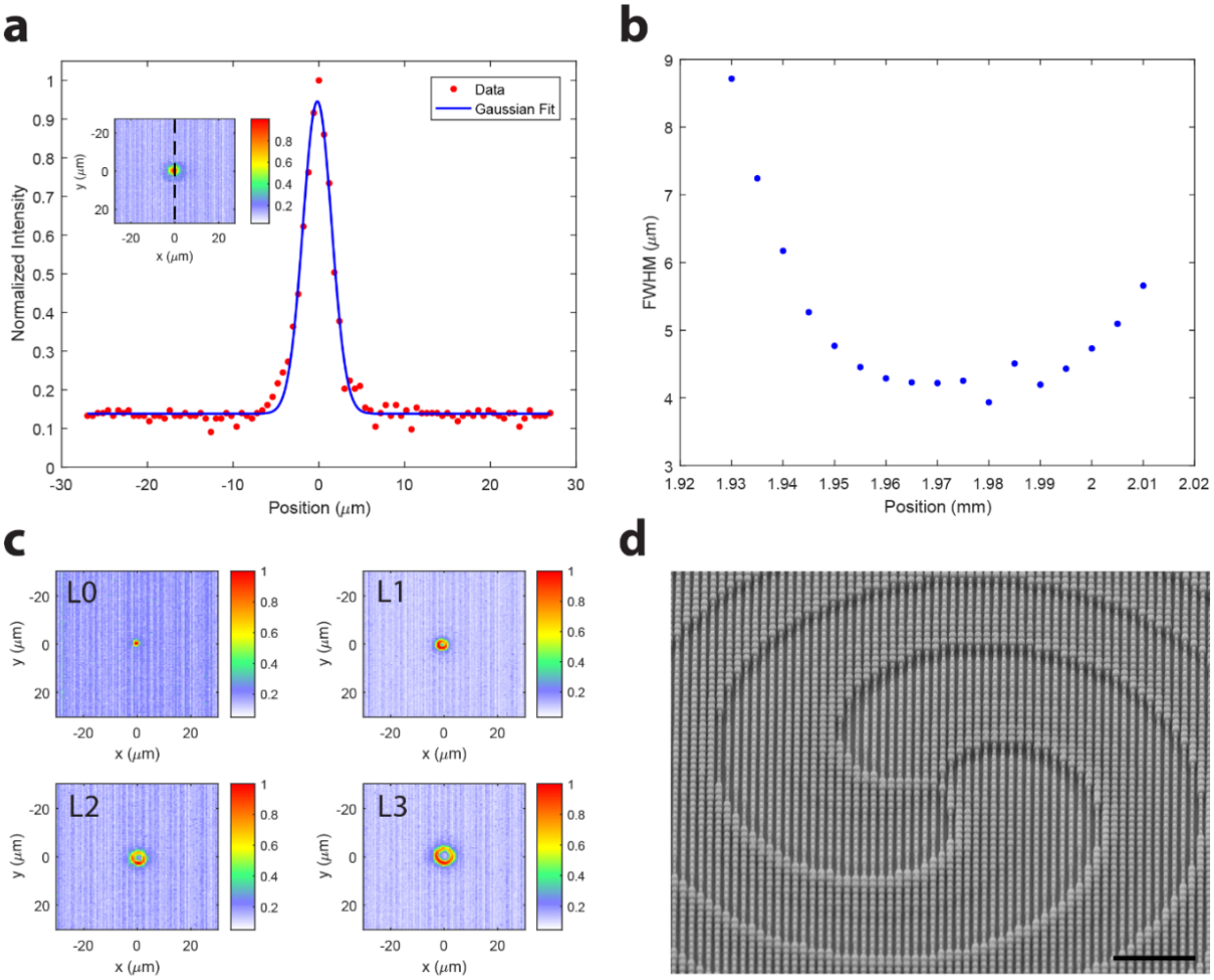

Fig. S1. Characterization of static metasurface aspherical and vortex beam-generating lenses for 1550 nm wavelength. (a) Cross section of a measured intensity profile at the focal plane of a designed static 2 mm focal length lens with 1 mm diameter using our nanoposts. The inset shows the 2D profile where the black dashed line indicates the position of the cross section. (b) Beam spot size in terms of full width at half maximum as a function of position along the optical axis of our lens from (a). (c) Measured cross sections at the focal plane of vortex beam-generating lenses, showing doughnut-shaped beams with different labelled values of topological charge. (d) 45° incident scanning electron micrograph of the L3 vortex beam lens. Scale bar 10 μm.

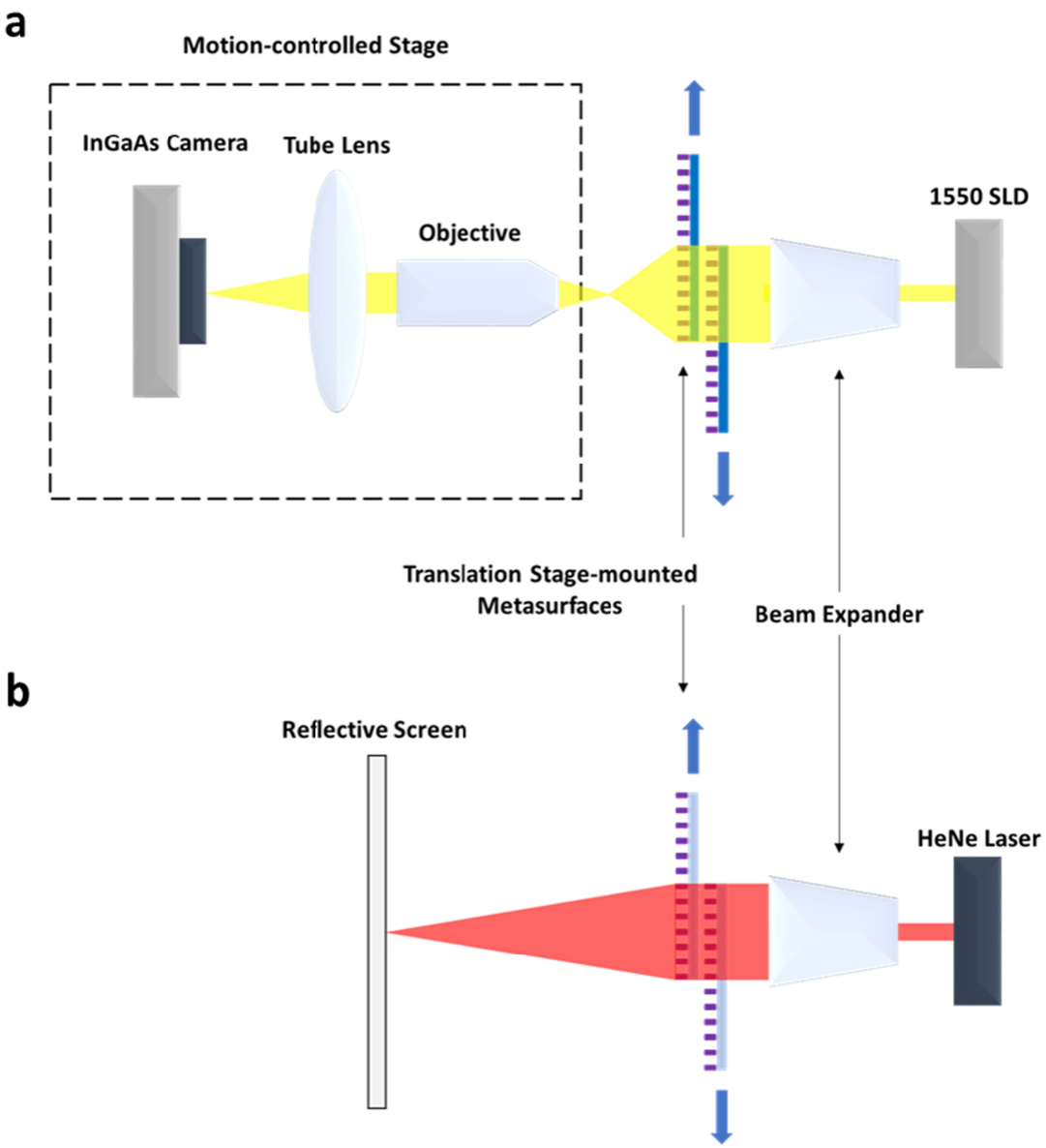

Fig. S2. Experimental setups for measuring the focal length of our tunable system. (a) Setup for measuring the focal length of our infrared tunable metalens. (b) Schematic of experimental setup for measuring the focal length of our visible wavelength tunable lens design.

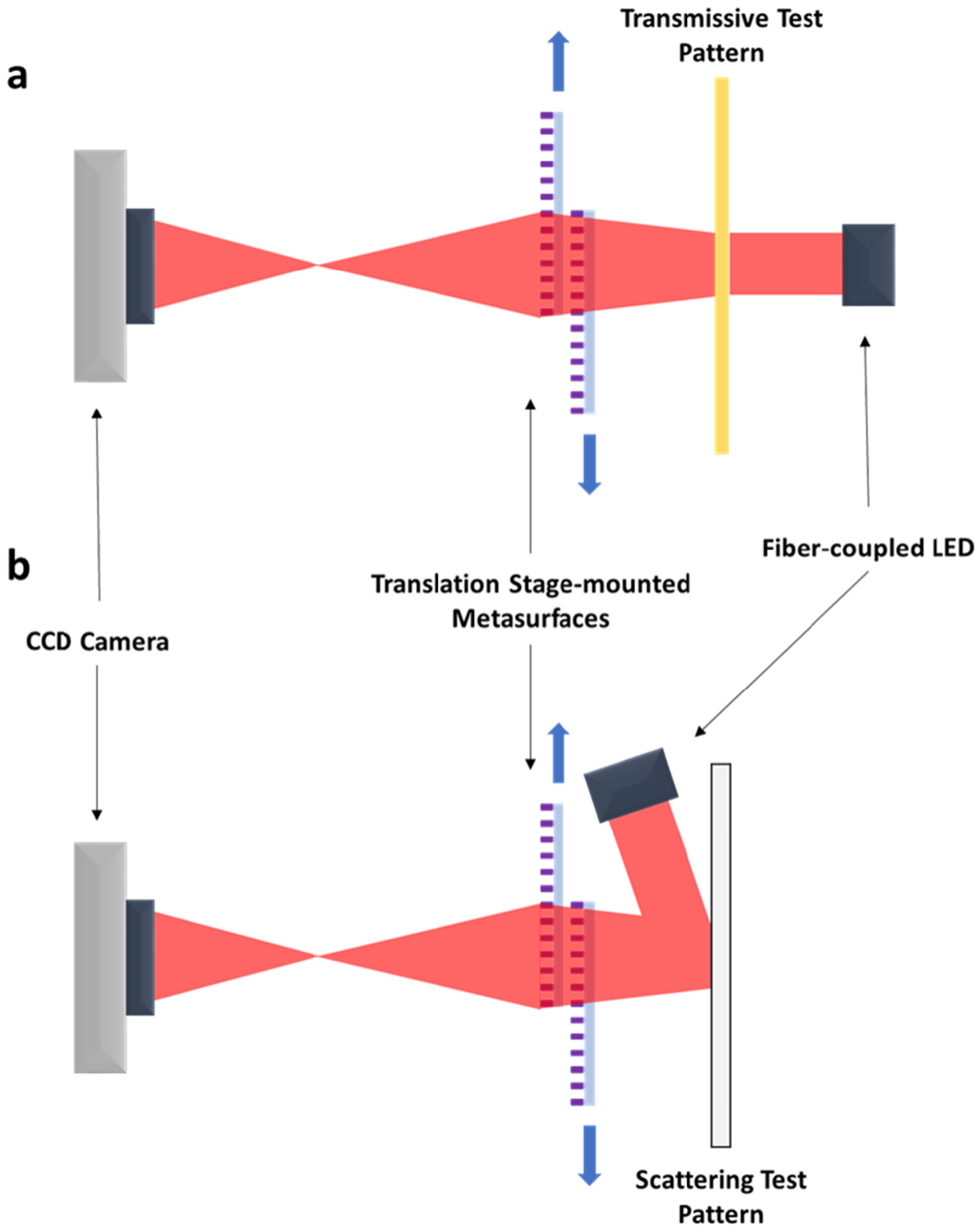

Fig. S3. Experimental setup for imaging experiments. We imaged object patterns in transmission (a) and by scattering light off objects (b) by projecting the image directly onto a camera without any additional magnification optics.

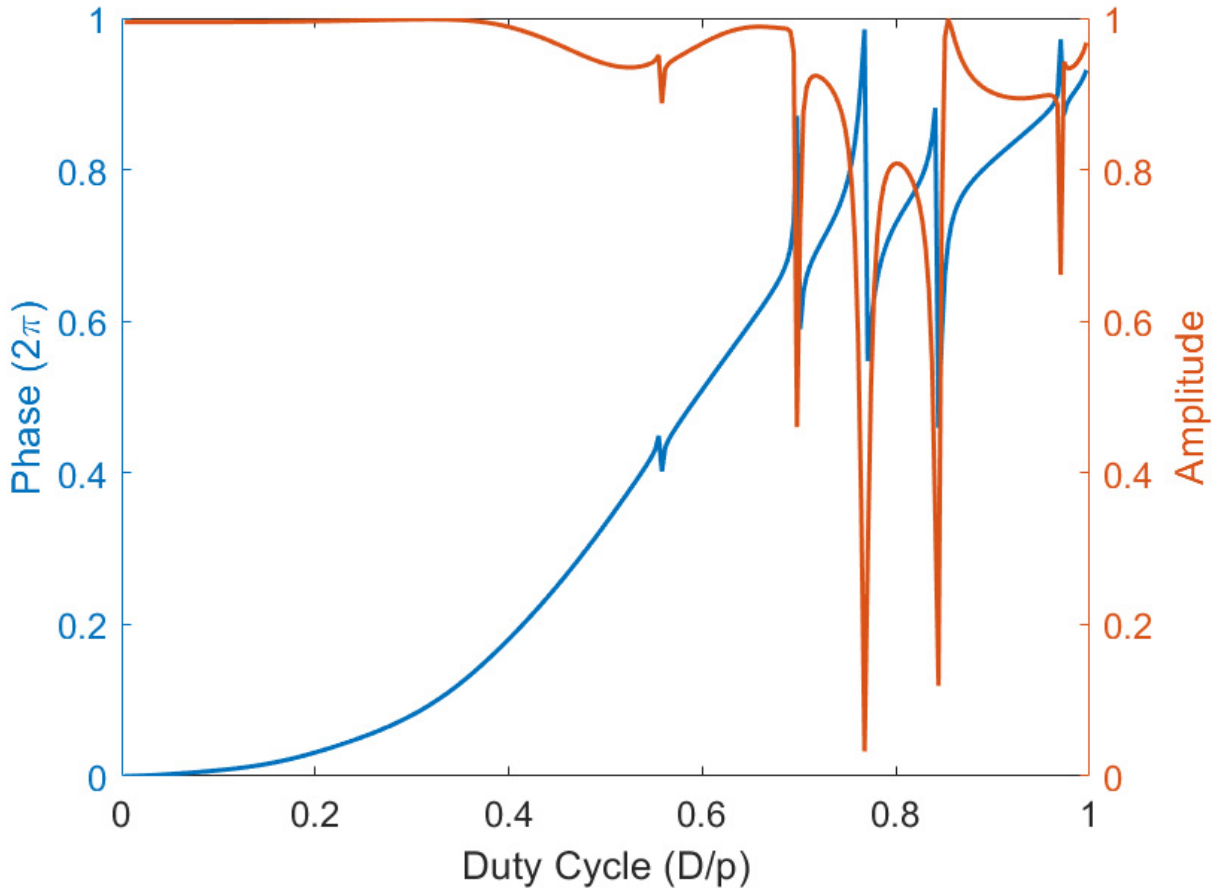

Fig. S4. DUV lithography-compatible silicon nitride nanopost design simulation. The simulated transmission coefficient is shown as a function of duty cycle. The nanopost is of thickness 633 nm and lattice constant 443 nm. By varying the post diameter between 125 nm and 400 nm, high efficiency metasurfaces can be realized.

References

1. V. Liu and S. Fan, "S4 : A free electromagnetic solver for layered periodic structures," Comput. Phys. Commun. **183**, 2233–2244 (2012).
2. N. Yu, P. Genevet, M. A. Kats, F. Aieta, J.-P. Tetienne, F. Capasso, and Z. Gaburro, "Light Propagation with Phase Discontinuities: Generalized Laws of Reflection and Refraction," Science **334**, 333–337 (2011).